Temporal Orthogonal Projection Inversion for EMI Sensing of UXO

Lin-Ping Song, *Member, IEEE*, Douglas W. Oldenburg, L. R. Pasion, S. D. Billings, and L. Beran

***Abstract*—We present a new approach for inverting time-domain electromagnetic data to recover the location and magnetic dipole polarizations of a limited number of buried objects. We form the multichannel electromagnetic induction (EMI) sensor data as a spatial–temporal response matrix (STRM). The rows of the STRM correspond to measurements sampled at different time channels from one sensor and the columns correspond to measurements sampled at the same time channel from different sensors. The singular value decomposition of the STRM produces the left and right singular vectors that are related to the sensor and the temporal spaces, respectively. If the effective rank of the STRM is r, then the first r singular vectors span signal subspaces (SS), and the remaining singular vectors span the noise subspaces. The original data are projected onto the SS, and the temporal orthogonal projection inversion (TOPI) uses these data in a nonlinear inverse problem to solve for source locations of the objects. The polarizations of the targets are then obtained by solving a linear optimization problem in the original data domain. We present theoretical and numerical analyses to investigate the singular value system of the STRM and the sensitivity of the TOPI to the size of an SS. Only a few subspace vectors are required to generate locations of the objects. The results are insensitive to the exact choice of rank, and this differs from usual methods that involve selecting the number of time channels to be used in the inversion and carefully estimating associated uncertainties. The proposed approach is evaluated using the synthetic and real multistatic EMI data.**

***Index Terms*—Electromagnetic induction (EMI), magnetic dipole polarization, nonlinear inversion, orthogonal projection, subspace, unexploded ordnance (UXO).**

I. Introduction

ELECTROMAGNETIC induction (EMI) sensing is a major survey in environmental remediation of unexploded ordnance (UXO) contamination [1]–[29]. Its effective use relies upon the ability to extract accurate target signatures (e.g., dipolar polarizabilities) from measured data. Those polarizabilities are subsequently used to discriminate UXO from nonhazardous clutter [20]–[22].

EMI signal processing is generally cast as a nonlinear overdetermined inverse problem, where the location of an object and its principal polarizations are sought [6]–[8], [12], [13], [23]–[29]. Data are acquired as a series of transient responses from an array of sensors. The noise level in the time channels vary, and later times are often particularly contaminated. A quality inversion thus begins with choosing which time channels should be included in the inversion and providing an assessment of expected noise. However, this issue has received little direct attention (see, for example, [6]–[13] for a single object case or [23]–[29] multiple objects). The general approach uses the hypothesis that responses at early time channels likely have a higher signal-to-noise ratio (SNR) and a simple selection of early time channels might be empirically set up for one type of sensor or particular data. If there are *a priori* estimates of the unknown sensor noise, one may also choose responses above a predefined SNR threshold in order to avoid possible adverse effects of late time noisy measurement on the estimated source parameters. Overall, however, the quality of the inversion result from inclusion of noisy data is most likely degraded unless accurate error estimates are available and proper weighting is chosen [8], [12], [13], [28].

In this paper, we present a method that is less dependent upon *a priori* noise estimates. We first define the spatial–temporal response matrix (STRM). This is the data matrix whose rows correspond to measurements at different time channels from one sensor (i.e., a single transmitter–receiver pair). Namely, each row is the time-domain decay curve for a particular sensor. The columns of the STRM are measurements at all sensors at a single time. The singular value decomposition (SVD) of this matrix provides a well-defined set of vectors with which to expand the rows of the STRM. We project the time-domain decay curves onto a small subspace by keeping only those vectors associated with larger singular values. A nonlinear inversion is then carried out in the transformed domain to find the source locations. The procedure, which we refer to as temporal orthogonal projection inversion (TOPI), has some advantages over the usual inversion method. Briefly, the TOPI uses the concept of subspace to select channels. There is no involvement of either the empirical selection of channels or a formidable task of estimating unknown noise. In addition, the subspace projection has the potential for separating signal from additive Gaussian noise and thus higher quality and more robust solutions are obtained in the inverse problem. Most importantly, the TOPI is insensitive to determining the dimension of the signal subspace (SS) and is able to recover accurate source locations using a small number of temporal projections. This further reduces the size of the inverse problem and speeds up the convergence. Once good estimates are obtained for the locations of the targets, their polarizabilities are subsequently

Manuscript received July 18, 2013; revised December 4, 2013 and March 10, 2014; accepted June 17, 2014. Date of publication July 15, 2014; date of current version August 12, 2014. This work was supported by the Strategic Environmental Research and Development Program under Grant MR-1629 and Grant MR-2318.

L.-P. Song and D. W. Oldenburg are with the Department of Earth, Ocean and Atmospheric Sciences, University of British Columbia, Vancouver, BC V6T 1Z4, Canada (e-mail: lpsong@eos.ubc.ca).

L. R. Pasion, S. D. Billings, and L. Beran are with the Black Tusk Geophysics Inc., Vancouver, BC V6J 4S5, Canada.

Color versions of one or more of the figures in this paper are available online at http://ieeexplore.ieee.org.

Digital Object Identifier 10.1109/TGRS.2014.2332992

obtained by solving a linear optimization problem in the original data domain.

The remaining parts of this paper are organized as follows. In Section II, we present the mathematical foundation for working with data from dipole models and outline our existing nonlinear inversion algorithm. In Section III, we present the SVD analysis of the STRM that relates spatial and temporal singular bases to the physical field quantities and derive our projection inversion method. In Section IV, we evaluate and discuss the technique using synthetic and real data recorded by the new-generation sensor array systems of the Time-domain Electro-Magnetic multi-sensor Towed Array Detection System (TEMTADS) [32]. Section V gives the conclusion.

II. Signal Model

A. Polarizability Tensor and Formulation

For a UXO survey, where the target dimension is often small relative to the target-sensor distance, the primary fields around the target can be approximately uniform, and the induced eddy currents in the target are localized and dominantly produce dipole responses [33], [34]. As a leading order approximation, the transient scattering of a metallic object can be well represented by an equivalent induced dipole. This dipolar dynamic property is characterized by a 3 × 3 symmetric magnetic polarizability tensor (MPT) $P(t)$ [1]–[12]

$$P(t) = \begin{bmatrix} p_{11}(t) & p_{12}(t) & p_{13}(t) \\ p_{12}(t) & p_{22}(t) & p_{23}(t) \\ p_{13}(t) & p_{23}(t) & p_{33}(t) \end{bmatrix} \tag{1}$$

where each element $p_{ij}(t)$ represents a dipole component in the ith Cartesian direction due to a primary field in jth Cartesian direction and where t is time. This polarizability tensor $P(t)$ has an eigendecomposition as

$$P(t) = \sum_{j=1}^{3} L_j(t)\mathbf{e}_j\mathbf{e}_j^T \tag{2}$$

where $\mathbf{e}_j (j = 1, 2, 3)$ is the orthonormal eigenvector representing the jth principal direction of dipolar polarization with respect to (w.r.t.) a reference system, superscript T denotes the transpose, and $L_j(t)$ is the principal polarization strength that is a function of the geometry and material of a target. In other words, $P(t)$ contains the information about the geometry and physical properties of a target, as well as its orientation. For axially symmetric objects, it is generally assumed that the principal directions are time independent. For an irregular shape object, the principal directions may vary with time [20]. However, in our inversion development, the assumption of time-independent principal directions is not critical since we work directly on the polarizability tensor $P(t)$ at each time channel rather than with its decomposition form of (2). This will be evident in the following description.

A typical survey uses multiple transmitter–receiver pairs. We assume M such pairs and denote the secondary response due to the ith Tx/Rx pair as d_i. This can be written in an inner product form w.r.t. $P(t)$, [1]–[12] as

$$d_i\left(\mathbf{r}_{Rx_i}, t\right) = \mathbf{a}_i^T\left(\mathbf{r}, \mathbf{r}_{Rx_i}, \mathbf{r}_{Tx_i}\right)\mathbf{q}(t) \tag{3}$$

where $\mathbf{a}_i(\mathbf{r}, \mathbf{r}_{Rx_i}, \mathbf{r}_{Tx_i})$ is 6 × 1 column vector representing spatial sensitivities of the ith sensor to the object located at $\mathbf{r}$, and $\mathbf{q}(t)$ a 6 × 1 column vector, whose components are the elements of the polarizability tensor $P(t)$ of an object. They are given by [27], [28]

$$\mathbf{a}_i\left(\mathbf{r}, \mathbf{r}_{Rx_i}, \mathbf{r}_{Tx_i}\right) = \begin{bmatrix} B_R^x B_T^x \\ B_R^x B_T^y + B_R^y B_T^x \\ B_R^x B_T^z + B_R^z B_T^x \\ B_R^y B_T^y \\ B_R^y B_T^z + B_R^z B_T^y \\ B_R^z B_T^z \end{bmatrix} \quad \mathbf{q}(t) = \begin{bmatrix} p_{11}(t) \\ p_{12}(t) \\ p_{13}(t) \\ p_{22}(t) \\ p_{23}(t) \\ p_{33}(t) \end{bmatrix} \tag{4}$$

where $[B_R^x\ B_R^y\ B_R^z]^T$ and $[B_T^x\ B_T^y\ B_T^z]^T$ are the Cartesian components of field vectors $\mathbf{B}_R(\mathbf{r}, \mathbf{r}_{Rx_i})$ and $\mathbf{B}_T(\mathbf{r}, \mathbf{r}_{Tx_i})$ that are generated at the object's location by the receiver and transmitter coils.

Assume that η objects are present in response to a given excitation. By neglecting EMI interaction between the objects [23]–[29], we model a measurement as a linear superposition of the signal from each object. That is, $d_i(\mathbf{r}_{Rx_i}, t) = \sum_{k=1}^{\eta} \mathbf{a}_i^T(\mathbf{r}_k, \mathbf{r}_{Rx_i}, \mathbf{r}_{Tx_i})\mathbf{q}_k(t)$, where $\mathbf{a}_i(\mathbf{r}_k, \mathbf{r}_{Rx_i}, \mathbf{r}_{Tx_i})$ defined in (4) are the spatial sensitivities of the ith sensor to the kth object located at $\mathbf{r}_k$ with polarizations $\mathbf{q}_k(t)$. The observed EMI responses for M sensors, in the presence of noise, can be conveniently expressed in a vector–matrix notation

$$\mathbf{d}(t) = \sum_{k=1}^{\eta} A(\mathbf{r}_k)\mathbf{q}_k(t) + \mathbf{n}(t) \tag{5}$$

where $\mathbf{d}(t) = [d_1(t), \ldots, d_M(t)]^T$ is an $M \times 1$ measured data vector at time t, $\mathbf{n}(t)$ is the additive noise vector, and $A(\mathbf{r}_k)$ is an $M \times 6$ matrix denoting the sensitivities of the M sensors to the kth object located at $\mathbf{r}_k$. Its transpose is given by

$$A^T(\mathbf{r}_k) = [\mathbf{a}_1(\mathbf{r}_k)\ \ldots\ \mathbf{a}_M(\mathbf{r}_k)]\,. \tag{6}$$

The position vectors of the sensor coils are suppressed in (5). It is understood that the sensor information is subscript indexed in the recordings and in the sensitivity vectors. Equation (5) is a generic dipole-based formulation for estimating and recovering the locations and polarizabilities of EMI anomalies. We note that for a single time channel of data and for a single object that we need at least $M > 9$ in order to have an overdetermined system. If there are η objects then $M > 9\eta$.

B. Two-Step Inversion

Here, we briefly review the sequential inversion algorithm of TEM data [27], [28] since we use this generic procedure throughout this paper to solve for locations and polarizations.

In the sequential inversion of η objects, the model parameters are grouped into two parts: a nonlinear part consisting of source locations $\mathbf{r} = \mathrm{vec}[\mathbf{r}_1, \ldots, \mathbf{r}_\eta]$ and a linear part consisting of source polarizations $\mathbf{q}(t) = \text{vec}[\mathbf{q}_1(t), \ldots, \mathbf{q}_\eta(t)]$ at time instant t. Here, vec$[\cdot]$ represents a vectorization operation, i.e., stacking all vectors into a single column. The use of notations $\mathbf{r}$ and $\mathbf{q}$ should be evident in the context of multiple objects. Denoting $A(\mathbf{r}) = [A(\mathbf{r}_1), \ldots, A(\mathbf{r}_\eta)]$ and using (5), we can write our full problem of determining $\mathbf{r}$ and $\mathbf{q}$ as a minimization of the functional given by

$$\min_{\mathbf{r},\mathbf{q}(t_j)} \sum_{j=1}^{N_t} \|W_j \left(\mathbf{d}_{\text{obs}}(t_j) - A(\mathbf{r})\mathbf{q}(t_j)\right)\|^2 \tag{7}$$

where N_t is the number of time channels used during this nonlinear update, and W_j is a diagonal data weighting matrix for the data at the selected time t_j. This is diagonal matrix with values equal to $1/\epsilon_i$, where ϵ_i is the estimated Gaussian uncertainty for each datum.

The parameter sets [see (5)] are separable because matrix $A(\mathbf{r}_k)$ is independent of source polarizations $\mathbf{q}_k(t)$. Thus, the data are a nonlinear functional of location coordinates of the object and a linear functional of the polarizations. Since the estimate of polarizations depends on the unknown locations, determining the two parameter sets simultaneously can make the problem more ill posed that requires a careful weighting for different scale sensitivity submatrices. In addition, it induces a difficult initial guess of polarizations. Rather, we solve (7) using a Gauss–Newton approach [35], [36], in which a step for finding updated target locations involves a linear inversion for polarizabilities as a subproblem.

At the nth iteration, we are provided with a location estimate $\mathbf{r}^{(n)}$ and polarizations $\mathbf{q}^{(n)}$. The linearized data equations, with a perturbation $\delta\mathbf{r}$, are

$$\mathbf{d}(\mathbf{r}^{(n)}+\delta\mathbf{r}, \mathbf{q}^{(n)}; t_j) = \mathbf{d}\left(\mathbf{r}^{(n)}, \mathbf{q}^{(n)}; t_j\right) + J\left(\mathbf{r}^{(n)}, \mathbf{q}^{(n)}; t_j\right)\delta\mathbf{r} \tag{8}$$

where $J(\mathbf{r}^{(n)}, \mathbf{q}^{(n)}; t_j) = (\partial A(\mathbf{r})/\partial \mathbf{r})|_{\mathbf{r}^{(n)}} \mathbf{q}^{(n)}(t_j)$ is the Jacobian and $A(\mathbf{r})$ is the composite matrix defined in (7).

At each iteration, we minimize

$$\min_{\delta\mathbf{r}} \sum_{j=1}^{N_t} \left\| W_j(\delta\mathbf{d}^{(n)}(t_j) - J^{(n)}(t_j)\delta\mathbf{r} \right\|$$
$$\text{subject to } \|\delta\mathbf{r}\| < \Delta \tag{9}$$

where $\delta\mathbf{d}^{(n)}(t_j) = \mathbf{d}_{\text{obs}}(t_j) - \mathbf{d}(\mathbf{r}^{(n)}, \mathbf{q}^{(n)}; t_j)$ and $J^{(n)}(t_j)$ is the current Jacobian. Δ is a positive scalar used to provide a local ball, within which $\delta\mathbf{r}$ is allowed to change w.r.t. the current $\mathbf{r}^{(n)}$ [35], [36]. This is generally a highly overdetermined system. The updated location is

$$\mathbf{r}^{(n+1)} = \mathbf{r}^{(n)} + \delta\mathbf{r}. \tag{10}$$

The polarizations $\mathbf{q}^{(n+1)}(t_j)$ needed for the next update are found by minimizing

$$\mathbf{q}^{(n+1)}(t_j) = \arg\min_{\mathbf{q}(t_j)} \left\|\mathbf{d}_{\text{obs}}(t_j) - A\left(\mathbf{r}^{(n+1)}\right)\mathbf{q}(t_j)\right\|^2$$
$$\text{s.t. } p_{k,ii}(t) \geq 0$$
$$|p_{k,il}(t)| \leq \frac{1}{2}\left[p_{k,ii}(t) + p_{k,ll}(t)\right], \quad i,l = 1,2,3 \tag{11}$$

where the constraints imposed on the polarizability elements p_{ij} arise from the symmetric positive definite matrix in (1) [37], [38].

The iterations in (9)–(11) are continued until convergence criteria are satisfied. This yields a set of final locations $\tilde{\mathbf{r}}_k$; polarizations $\tilde{\mathbf{q}}_k (k = 1, \ldots, \eta)$ are obtained by (11) for all time channels. Note that the solution for $\mathbf{q}_k(t)$ is solved at each time channel. The principal directions and polarizations might be simply obtained by the eigendecomposition of each individual MPT. There are no numerical restrictions or physical assumptions that these directions are identical or close to each other. As suggested in [28], an average principal direction can be sought across a range of times via a joint diagonalization of the polarizabiltiy tensors.

It is observed in (9) that the computed source locations depends upon the responses at N_t selected time channels. The issue of which time channels to select is the focus of the next section.

III. Method

A. STRM and Its SVD

EMI data are generally acquired with an array of sensors. Each sensor records data at times $t_1, \ldots, t_j$. Assuming M Tx/Rx pairs, we arrange data as

$$D = \begin{bmatrix} d_1(t_1) & \cdots & d_1(t_J) \\ \vdots & \vdots & \vdots \\ d_M(t_1) & \cdots & d_M(t_J) \end{bmatrix}. \tag{12}$$

We call this the STRM. Its rows correspond to responses sampled at different time channels from one transmitter/receiver pair and its columns to measurements sampled at the same time channel from different transmitter/receiver combinations. The STRM can be formed for a static or a dynamic survey with monostatic or multistatic array configurations.

The SVD [37], [38] of D in (12) is written as

$$D = U\Sigma V^T = \sum_{i=1}^{p} \sigma_{ii}\mathbf{u}_i\mathbf{v}_i^T \tag{13}$$

where $p = \min(M, J)$, $U = [\mathbf{u}_1, \ldots, \mathbf{u}_M]$ is an $M \times M$ left orthonormal matrix, $V = [\mathbf{v}_1, \ldots, \mathbf{v}_J]$ is a $J \times J$ right orthonormal matrix, and Σ is an $M \times J$ singular value matrix with elements σ_{ii} along the diagonal and zeros everywhere else. If the singular values are ordered so that

$$\sigma_{11} \geq \sigma_{22} \geq \cdots \sigma_{pp} \geq 0 \tag{14}$$

and if the matrix has a rank $r < p$, then the last singular values are equal to zero and the SVD of D becomes

$$D = \sum_{i=1}^{r} \sigma_{ii}\mathbf{u}_i\mathbf{v}_i^T. \tag{15}$$

Equations (13) or (15) hold w.r.t. any ordering of singular values and singular vectors and sign of each of the column pairs $\mathbf{u}_i$ and $\mathbf{v}_i$. With the decreasing ordering of singular values, as in (14), the SVD is unique up to a sign change of both left and right singular vectors.

To understand the SVD of D, we relate the triplet $\{\sigma_{ii}, \mathbf{u}_i, \mathbf{v}_i\}$ in (15) to field quantities A and $\mathbf{q}$. It is sufficient to consider data from a single object as given by (3). Replacing each entry in (12) with (3), we rewrite (12) as

$$D = A(\mathbf{r})Q^T \tag{16}$$

where $A(\mathbf{r})$ is an $M \times 6$ array response matrix defined in (6). Q^T is a $6 \times J$ source matrix

$$Q^T = [\mathbf{q}(t_1) \cdots \mathbf{q}(t_J)] \tag{17}$$

whose column corresponds to one temporal component of the dynamic polarizability tensor.

To generate an SVD form of (16), we introduce the two symmetric matrices [37]

$$W_A = (A^T A)^{\frac{1}{2}},\ W_Q = (Q^T Q)^{\frac{1}{2}}. \tag{18}$$

Using W_A and W_Q, we transform D in (16) into

$$D = AW_A^{-1} W_A W_Q \left(QW_Q^{-1}\right)^T. \tag{19}$$

Setting

$$U_A = AW_A^{-1},\ V_Q = QW_Q^{-1},\ X = W_A W_Q \tag{20}$$

taking the SVD of X as $X = U_X \Pi V_X^T$, we write (19) as

$$D = (U_A U_X)\Pi(V_Q V_X)^T \tag{21}$$

where $U_A^T U_A = I$ and $V_Q^T V_Q = I$. Equation (21) is an explicit form of SVD decomposition of D. The left singular vectors are the columns of $U_A U_X$, and the right singular vectors are the columns of $V_Q V_X$. The singular values of D are the diagonal entries of Π, i.e., the eigenvalues of the square matrix X.

With the previous discussion on the uniqueness of a SVD and comparing (21) to (15), we have

$$U_A U_{X,i} = \mathbf{u}_i \quad V_Q V_{X,i} = \mathbf{v}_i, \qquad i = 1, \ldots, r \tag{22}$$

where $U_{X,i}$ and $V_{X,i}$ represent the ith column of U_X and V_X. Equation (22) shows that for $\sigma_{ii} > 0$ the singular vectors $\mathbf{u}_i$ are linear combinations of the orthonormalized array Green's function matrix U_A and form an orthonormal basis spanning the sensor-target location space, whereas the singular vectors $\mathbf{v}_i$ are linear combinations of the orthonormalized polarizability source matrix V_Q and form an orthonormal basis spanning the temporal space. Both left and right singular vectors contain information of the target locations and polarizabilities. The former in principle can be used in MUSIC-like imaging to estimate target location [30]. However, in this development, our scope is concentrated on the use of the latter as a basis to project original temporal responses for inversion. Finally, there is no direct connection of Π with the principal polarizabilities of L_j. The eigenvalues of an STRM cannot be simply interpreted as apparent principal polarizabilities as in the multistatic response matrix that has measurements taken at one location and requires a sufficient number of transmitters and receivers [30], [31].

B. Rank of D

From SVD analysis, the data matrix D given in (12) has rank $r \le p = \min(M, J)$. However, we also have $D = AQ^T$ [see (16)]. From the matrix analysis theory [37], we have $\text{rank}(D) = \text{rank}(AQ^T) \le \min[\text{rank}(A), \text{rank}(Q^T)]$. Provided $M \ge 6$ and $J \ge 6$ then both $\text{rank}(A) \le 6$ and $\text{rank}(Q^T) \le 6$, this restricts the maximum rank of D for a single object to 6. Theoretically, if there are η objects contributing to the data then the maximum rank is 6η. This is for a general case, where principal directions might be rotational with time.

For the case that the principal coordinates of the polarizability matrix are time independent, Q^T is controlled by three parameters L_j. Using (2), we can express Q^T as $Q^T = EL$ where E is a 6×3 matrix whose elements are related to the principal direction vectors $\mathbf{e}_j$ and L is a $3 \times J$ matrix whose elements are the three principal polarizabilties in J time channels. By applying the rank inequality property, we have $\text{rank}(Q^T) = \text{rank}(EL) \le \min[\text{rank}(E), \text{rank}(L)] \le 3$ provided $J \ge 3$. Thus, the maximum rank of Q is 3 if the data are from a single object. That rank can be reduced to 2 for a cylindrically symmetrical object that has two distinct principal polarizabilities, or to rank one for a sphere. In general, if there are η objects contributing to the data, then the maximum rank is 3η.

C. Temporal Orthogonal Projection and Inversion

Assuming that the matrix has a rank r, as described in (15), we group these SVD-constructed orthonormal vectors into the left and right SS, i.e., $U_s = [\mathbf{u}_1, \ldots, \mathbf{u}_r]$ and $V_s = [\mathbf{v}_1, \ldots, \mathbf{v}_r]$. The remaining singular vectors, $U_n = [\mathbf{u}_{r+1}, \ldots, \mathbf{u}_M]$ and $V_n = [\mathbf{v}_{r+1}, \ldots, \mathbf{v}_M]$, are correspondingly grouped as the left and right orthonormal noise subspaces (NS).

Next, we project the data onto V_s. Right-multiplying (16) with submatrix V_s, we have

$$D_s = A(\mathbf{r})Q_s^T \tag{23}$$

where

$$D_s = DV_s \tag{24}$$

is a projected data matrix of $M \times r$ and

$$Q_s^T = Q^T V_s \tag{25}$$

is a projected source matrix of $6 \times r$ for a single-object case. Equation (23) is a temporal orthogonal projection equation, where the original J time channels are converted into r SS temporal channels but the sensitivity matrix A remains unchanged. For numerical implementation of an inversion in the

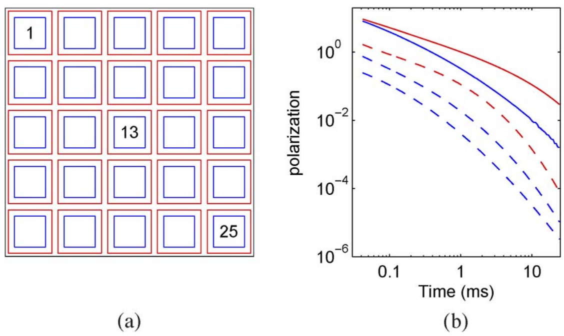

Fig. 1. (a) TEMTADS: a single-component multistatic system consisting of a horizontally arranged coplanar array of 5 × 5 transmitters and receivers. Each transmitter is 35 cm × 35 cm and each receiver 25 cm × 25 cm. (b) Two sets of polarizations used for the numerical experiments. The solid and dashed curves represent polarizations of a 105-mm projectile and a scrap item, respectively.

transformed domain, (23) might be rewritten as a matrix-vector form for each projected temporal channel i

$$\mathbf{d}_s(i) = \sum_{k=1}^{\eta} A(\mathbf{r}_k)\mathbf{q}_{s,k}(i) + \mathbf{n}_s(i), \qquad i = 1, \ldots, r \qquad (26)$$

where $\mathbf{d}_s(i) = [d_{s,1}(i), \ldots, d_{s,M}(i)]^T$ is an $M \times 1$ projected data vector at projected channel i, $\mathbf{n}_s(i)$ is the projected noise vector. Considering the decomposition of (15) and the orthonormality of vectors $\mathbf{v}_i$, we can see that projected data $\mathbf{d}_s(i) = \sigma_{ii}\mathbf{u}_i$. Namely, σ_{ii} controls the importance of the ith normalized channel $\mathbf{u}_i$.

Like the original domain (5), the transformed (26) retains the feature that $\mathbf{d}_s$ is linear w.r.t. source parameter $\mathbf{q}_s$ and nonlinear w.r.t. the locations of objects. Therefore, the same solution strategy outlined in Section II-B can be applied to (26) by replacing $\mathbf{d}$ and $\mathbf{q}$ with $\mathbf{d}_s$ and $\mathbf{q}_s$ in (9). The statistics of the projected noise are difficult to evaluate, but we make the much-used assumption for now that the noise is Gaussian and uncorrelated and that each datum has the same standard deviation. Thus, the data weighting matrix in (9) becomes a scaled identity matrix. We now proceed with the TOPI where the r SS projected temporal channels are used to localize sources via the nonlinear update. Once source locations are determined, the target polarizabilties are solved as a linear optimization problem in the original data domain via (11). The orientation of each object, if desired, can be extracted from the polarizability tensors, according to the method outlined in Section II-B [28].

IV. Experiments

An important question for the TOPI concerns the size of the subspace used and the nature of the associated basis vectors. To illustrate the relationship between the rank and the polarizations of an object, and divisions between SS and NS, we perform experiments using synthetic and real TEMTADS data. TEMTADS [32] is a single-component multistatic system. It consists of a horizontally arranged coplanar array of 5 × 5 transmitters and receivers [see Fig. 1(a)]. The sizes of its transmitters and receivers are 35 cm × 35 cm and 25 cm × 25 cm, respectively. Data are acquired at 115 logarithmically spaced channels between 0.042 and 24.35 ms. For each transmitter excitation, TEMTADS records the response at all receivers. Thus, it has spatial–temporal data of 625 × 115 for a static (cued) survey. Fig. 1(b) shows the two sets of polarizations that will be used for the numerical experiments. The solid and dashed curves represent polarizations of a 105-mm projectile and a scrap item, respectively. In the following numerical experiments with TEMTADS, we specify the number, location, and orientation of the objects and their polarizations. We assume that the principal directions are time independent. Given these simulation parameters, we are able to calculate sensitivity matrix $A(\mathbf{r}_k)$ and form polarization parameter vector $\mathbf{q}_k(t)$. It is then straightforward to generate synthetic signals, ranging from 0.042 to 24.35 ms, in the absence or presence of noise using (5).

For all inversion experiments either in the original domain or with the TOPI, we use the multistart strategy to initialize an inversion(for details see [28]). Briefly, the initialization process consists of the following:

1) Creating a few hundred (e.g., 300) random trial locations for η objects within the region of interest.
2) Evaluating these trial locations within a single linear inversion to generate polarizabilities and rank the trials according to their achieved misfits.
3) Selecting a few (e.g., 5) distinct trial locations that have low misfits as starting locations for a nonlinear update. Among multiple nonlinear solutions, the one with the smallest misfit is chosen as the set of final locations.

A. Synthetic Single-Object Example

For an experiment with a single object, we consider a 105-mm projectile-like object buried at $(0, 0, -0.60)$ m and vertically oriented. Fig. 2(a) is a plot of the singular values versus their indexes for the noise-free case. Two sets of singular values, calculated from matrices D (denoted as circles) and X (denoted as crosses) in (20), are shown. The projectile has circular symmetry and hence, from our earlier analysis, the rank should be equal to 2. It is observed that there are only two large singular values and that those of D and X are equal, as they were shown to be in Section III. This numerically illustrates that the signal singular values of STRM D are governed by those of X. The other small nonzero singular values evident in Fig. 2(a) are a consequence of numerical noise.

To see how additive noise affects the singular values, we add 3%, 5%, and 10% Gaussian noise to the synthetic data. As shown in Fig. 2(b)–(d), this noise lifts the small nonzero singular values to a level that might be comparable to singular values of signal. In this example, however, the signal singular values are still distinguishable with 10% noise given the ground truth and suggest that the rank of D is 2. However, in reality, the number of targets and their geometries are unknown, there could be an ambiguity to determine the true rank of D. For instance, Fig. 2(d) can also suggest that the rank of D is at least two and a third nonzero singular value might represent signal singular value that looks likely hidden in the noise.

Additional insight about the rank of the matrix can be gleaned from the shape of the singular vectors in V. We refer

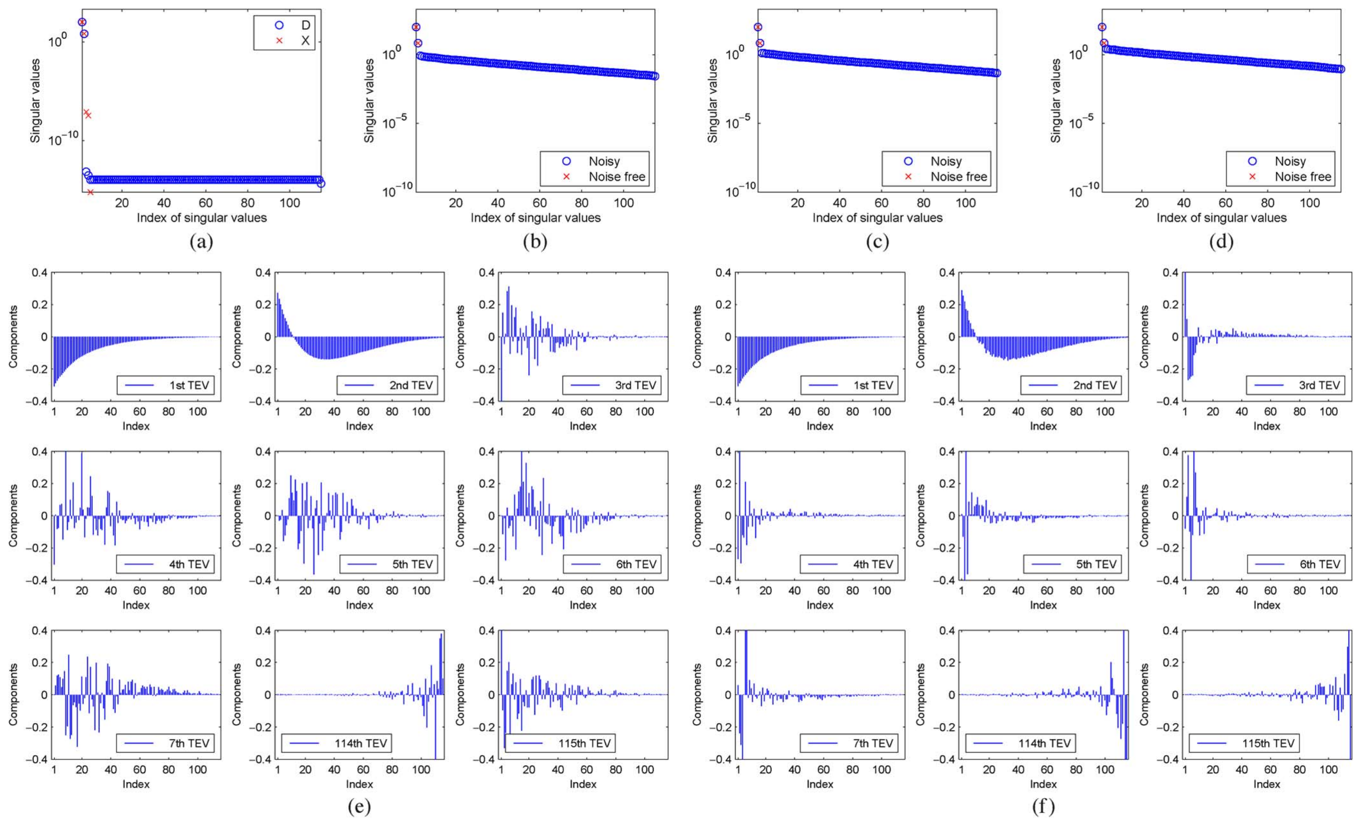

Fig. 2. Single-object case. Singular values: (a) noise free; (b) 3% noise; (c) 5% noise; and (d) 10% noise. The first seven and the last two TEVs: (e) noise free and (f) 10% noise.

to these as temporal eigenvectors (TEVs). Fig. 2(e) shows the first seven and the last two TEVs in V for noise-free case. The first two vectors are smooth, and they span the 2-D SS. The remaining singular vectors, which span the NS, have a random behavior. The TEVs for 10% additive noise are shown in Fig. 2(f). The first two TEVs have almost the same structure as in the noise-free case but the remaining vectors are substantially different and are characterized by high frequency fluctuations. The number of smooth TEVs corresponds to the rank of two. In this noisy case, the singular vectors that are smooth and show progressively more zero crossings are more diagnostic in determining the rank of the D than solely inspecting singular value distribution.

With the SVD decomposition, and knowledge of the rank of the matrix, we can generate our SS and NS. To illustrate the effectiveness of this, we carry out an analysis using 10% noise. Fig. 3(a)–(c) show the true noise-free decay signals, the random noise, and the corrupted signals produced at all 625 Tx/Rx pairs. Using the triplets of $\{\sigma_{ii}, \mathbf{u}_i, \mathbf{v}_i\}$ derived from the corrupted signals, we want to reconstruct the noise-free data using $\tilde{D} = \sum_{i=1}^{2} \sigma_{ii}\mathbf{u}_i\mathbf{v}_i^T$ where the rank is 2. The remaining eigenvalues and eigenvectors can be used to estimate noise as $\tilde{N} = \sum_{i=3}^{115} \sigma_{ii}\mathbf{u}_i\mathbf{v}_i^T$. As a measure of accuracy, we compute a relative error defined as $\delta = \|D_{\mathrm{true}} - \tilde{D}\|_F / \|D_{\mathrm{true}}\|_F$ where $\|\cdot\|_F$ denotes the Frobenius norm [38]. Fig. 3(d) shows the estimated data $\tilde{D}$. By comparing with the noise-free signals in Fig. 3(a), we observe that the additive noise has been substantially reduced. The approximation error of $\delta = 2.5\%$ is much less than the noise level of 10%. Fig. 3(e) shows the estimated noise. These results show that the subspace concept can be a useful tool for separating signal from unwanted noise.

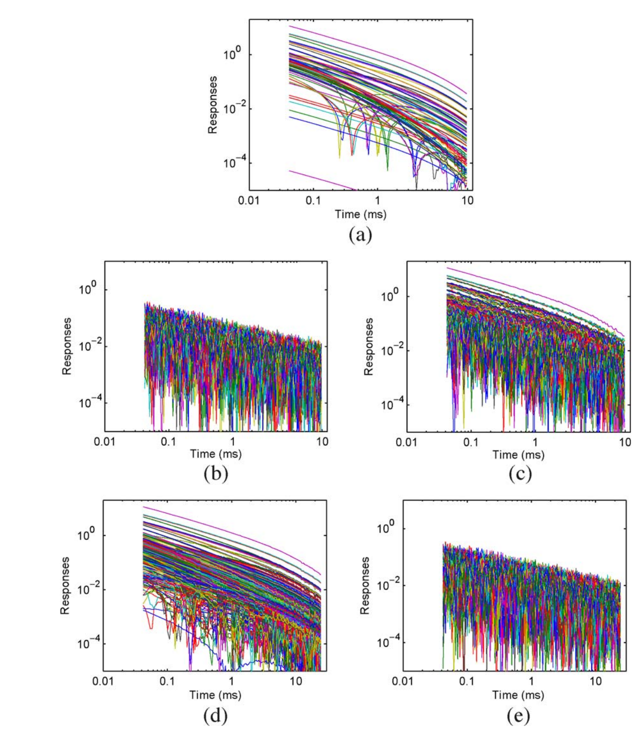

Fig. 3. Single-object case. For all 625 Tx/Rx pairs. (a) Noise-free decay signals. (b) Noise (10%). (c) Corrupted signals = (a) + (b). (d) Estimated signal. (e) Estimated noise.

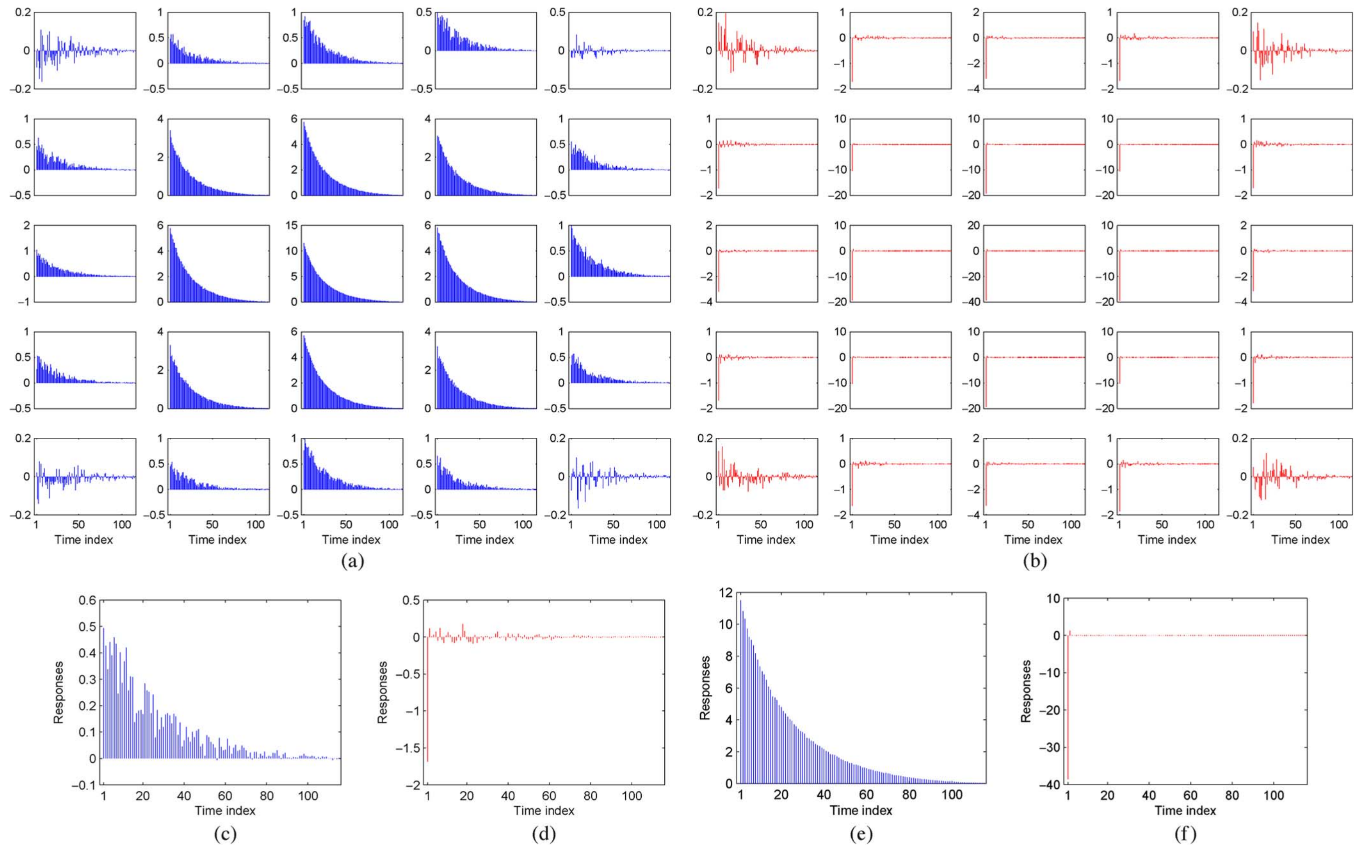

Fig. 4. Single-object case. 10% Noise. (a) Original data at 25 receivers with Tx-13 excitation. (b) Projected data at 25 receivers with Tx-13 excitation. (c), (d) Original and projected data of Tx-13/Rx-4 pair. (e), (f) Original and projected data of Tx-13/Rx-13 pair.

The last item to explore within the decomposition concerns the projected data. As an example, Fig. 4 shows the data for Transmitter 13. The projection of these data onto the space spanned by vectors V_s and V_n is also shown in that figure. The projected data consist of a few large values that correspond to the larger singular values and small random values thereafter. This character is easily understood. The first singular vector $\mathbf{v}_1$ is a smoothly decaying single polarity curve. Its character is similar to the data observed at many Tx/Rx pairs. Hence, the inner product of that basis with the rows of D generates a large value. Inner products with other vectors that have additional zero crossings will yield smaller data values. Eventually, inner products with highly variable vectors, and especially when those vectors have increasing amplitudes at larger times, produce projected data that contain little information and whose uncertainty greatly exceeds their values.

Let us turn to the TOPI based on (26) for the 10% noise case. We have determined that the rank of D for this single object is 2. As such, we now run the TOPI using the two projection vectors $\mathbf{v}_1$ and $\mathbf{v}_2$. The inversion returns an almost exact location $\mathbf{r} = (0.00, -0.01, -0.60)$ m. In fact, we can obtain the same result when we run the TOPI with only $\mathbf{v}_1$ or only $\mathbf{v}_2$. Each of these signal vectors contains enough information to allow recovery of the location. This arises because we have 625 data for each time channel, and hence, the problem is still overdetermined even with a single time channel of data. It is important that the vectors chosen for TOPI are signal vectors or at least the subspace used contains signal vectors. To illustrate this point, we run the TOPI with the vector $\mathbf{v}_3$, which is a singular vector corresponding to the NS. The TOPI gives $\mathbf{r} = (0.61, 1.00, -1.20)$ m, which is a meaningless result. Finally, we carry out the inversion using the first three and then the first five vectors. Both of these inversions, which include signal vectors plus noise vectors, produce the same results $\mathbf{r} = (0.00, -0.00, -0.60)$ m. Removing $\mathbf{v}_1$, we conduct the TOPI using the two subspaces of $[\mathbf{v}_2, \mathbf{v}_3]$ and $[\mathbf{v}_2, \ldots, \mathbf{v}_5]$, respectively. Both the tests still deliver the location at $\mathbf{r} = (0.00, -0.01, -0.60)$ m. The experiments demonstrate that the TOPI is stable whenever signal vectors are used to project data. Of course, this still requires that M is large enough so that the problem is overdetermined.

B. Synthetic Two-Object Example

For a two-object example, we place a shallow object at $\mathbf{r}_2 = (0.03, -0.01, -0.09)$ m and a deep object, a 105-mm projectile, at $\mathbf{r}_1 = (0, 0, -0.60)$ m. The shallow object is horizontally oriented and the deep object is vertical. This simulates a practical scenario, where a piece of scrap is often buried at a shallow depth and a large UXO can penetrate into deep ground. Both polarizabilities are given in Fig. 1(b). Different levels of Gaussian noise have been added to the data prior to input into the SVD. For the noise-free case, Fig. 5(a) shows that both D and X have the five identical larger singular values. That is the number of distinct polarizabilities effected from a symmetric ordnance and a scrap. The remaining singular values of X

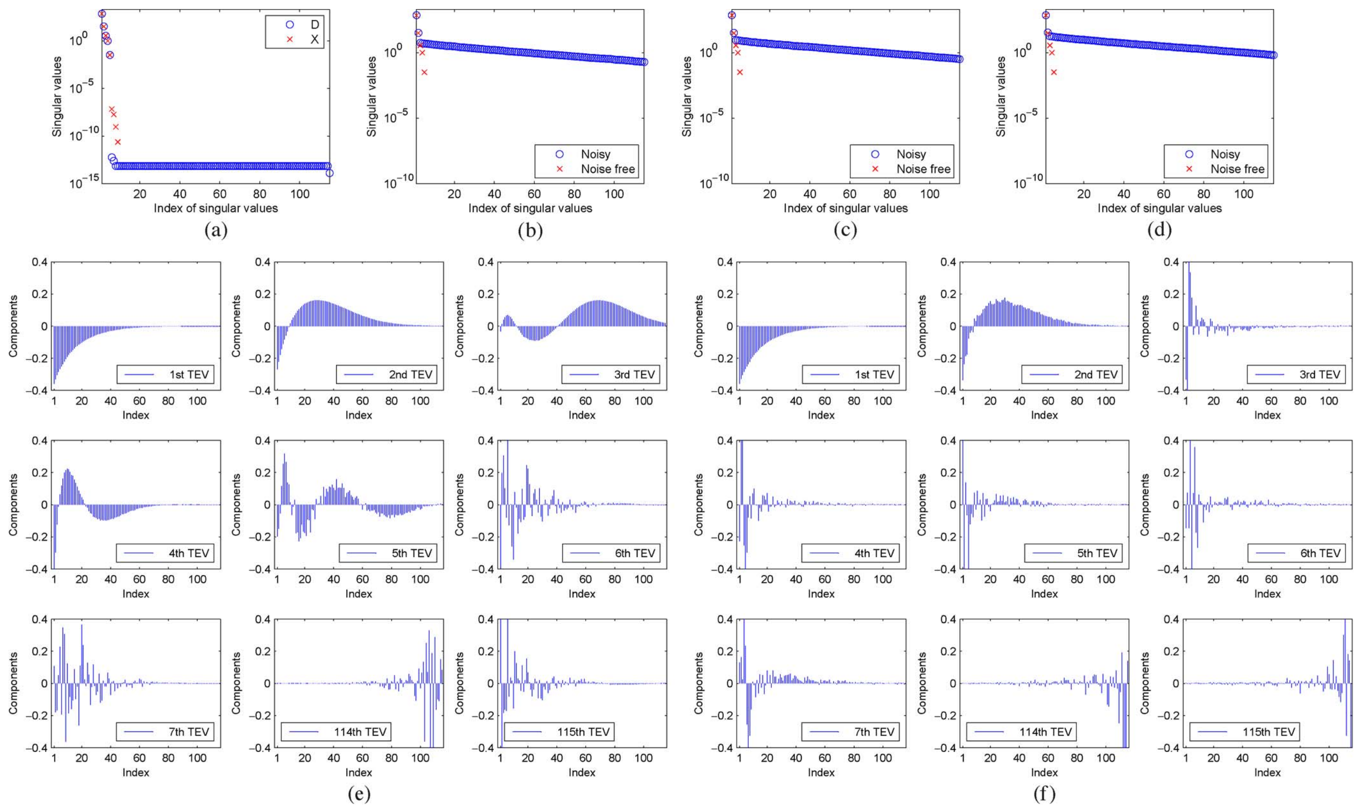

Fig. 5. Two-object case. Singular values: (a) noise free; (b) 3% noise; (c) 5% noise; and (d) 10% noise. The first seven and the last two TEVs: (e) noise free and (f) 10% noise.

and D, which ideally should be zero, are numerically small. The first five singular vectors are smooth and progressively display more zero crossings, whereas the other singular vectors behave randomly [see Fig. 5(e)]. Based upon these eigencharacteristics, one can define that the maximal dimension of the SS is 5 in this case. The rank of D in this case is 5. The situation changes when noise is added. Corrupting the data with 3%–10% noise produces singular values shown in Fig. 5(b)–(d). The result is similar to that with a single object, where the addition of noise lifts the singular values. The three smaller signal singular values, observed in the noise-free case, are now buried in the noise. The ideal SS is also distorted by the noise. The singular vectors in Fig. 5(f) associated with the three small signal singular values become oscillatory and behave like noise eigenvectors. Therefore, in these noisy examples, the effective rank, or the reduced SS of the data D, is 2 if we determine rank in terms of the significant singular values and associated smooth eigenvectors. This experiment illustrates that, in practice, one should be cautious about inferring the number of objects using a singular value spectrum.

To test the aforementioned analysis about the singular values/vectors for the 10% noise case, we first project the original signals using individual eigenvectors $\mathbf{v}_1$, $\mathbf{v}_2$, and $\mathbf{v}_3$ and the implement the TOPI, respectively. With $\mathbf{v}_1$ projection, the TOPI returns $\mathbf{r}_1 = (0.00, -0.00, -0.61)$ m and $\mathbf{r}_2 = (0.03, -0.01, -0.09)$ m. With the projected channel at $\mathbf{v}_2$, the TOPI returns $\mathbf{r}_1 = (0.02, 0.02, -0.61)$ m and $\mathbf{r}_2 = (0.04, -0.02, -0.08)$ m. The inverted locations of the objects in both cases are almost the same and close to the true values. However, using $\mathbf{v}_3$ alone in the TOPI yields $\mathbf{r}_1 = (0.43, -0.81, -0.72)$ m and $\mathbf{r}_2 = (0.43, -0.81, -0.72)$ m. These are far from the true locations. Referring back to Fig. 5(f), we see that $\mathbf{v}_3$ is a severely contaminated signal vector in contrast to the noise-free $\mathbf{v}_3$ in Fig. 5(e). Thus, the inversion with $\mathbf{v}_3$ might be expected to be worse. The TOPI experiment demonstrates that the effective rank is 2, and this is consistent with the singular spectrum analysis. Nevertheless, this effective rank value cannot be used to infer that there is only a single object.

Next, we evaluate the TOPI using the channels projected onto the three subspaces of $[\mathbf{v}_1, \ldots, \mathbf{v}_j] (j = 2, 5, 10)$, respectively. These three subspaces contain the common signal eigenvectors $\mathbf{v}_1$ and $\mathbf{v}_2$. Not surprisingly, all inversions give almost exact results at $\mathbf{r}_1 = (0.00, -0.00, -0.61)$ m and $\mathbf{r}_2 = (0.03, -0.01, -0.09)$ m. These tests show that, like the single-object case, the TOPI is robust to a rank determination or a SS dimension if signal eigenvectors are included in the projection process. This numerical property of the TOPI is further illustrated in the following experiment.

By including more eigenvectors, we extend the aforementioned tested subspace into $[\mathbf{v}_1, \ldots, \mathbf{v}_{39}]$. Projecting the original noisy data onto this subspace, running the TOPI with the 39 projected channels, we again obtain almost exact locations at $\mathbf{r}_1 = (0.00, -0.00, -0.61)$ m and $\mathbf{r}_2 = (0.03, -0.01, -0.09)$ m. The time taken to invert with 39 projected time channels was 0.13 min. We now compare these results with the inversion in the original data domain. The challenge with working in the original domain is deciding how many and which time channels to use. Certainly, late time channels can be problematic, but it is difficult to decide where to make the cut. Here, we estimated that the first $N_t = 39$ time channels with time ranging from $t_1 = 0.042$ ms to $t_{39} = 0.469$ ms could be used. With this subset, the inversion yields $\mathbf{r}_1 = (0.00, -0.01, -0.35)$ m and $\mathbf{r}_2 = (0.14, -0.01, -0.02)$ m, which is a rather poor result; it also took 1.20 min. It is possible that different choices of time channels can still produce a good result. For instance, using the first $N_t = 10$ time channels produced the good locations at $\mathbf{r}_1 = (0.00, -0.00, -0.61)$ m and $\mathbf{r}_2 = (0.03, -0.01, -0.09)$ m). In the TOPI, we use all 115 time channels to construct TEVs. To be comparable to the TOPI, we tested the original data domain inversion using $N_t = 115$ time channels. The inversion gives $\mathbf{r}_1 = (-0.01, -0.00, -0.45)$ m and $\mathbf{r}_2 = (0.03, -0.01, -0.04)$ m). The inverted horizontal locations of the two objects are good. However, their inverted depths are shallower, shifted by -0.15 and -0.05 m as compared with true ones. It took 1.73 min. Unlike the TOPI, the simple use of all time channels in an inversion does not provide an optimal solution. The advantage of the TOPI is that much of the previous guessing about which time channels to use is removed, and the inversion with a few signal channels provides a more robust methodology. We next proceed with a real data example.

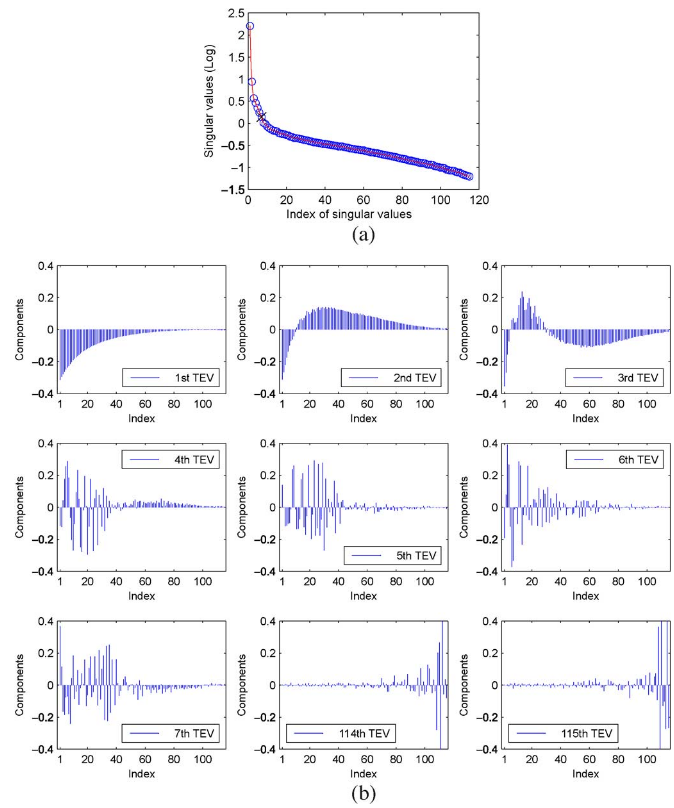

Fig. 6. Test-pit data. (a) Singular values. (b) The first seven and the last two TEVs.

C. Real Data Example

For a real data example, we use the test-pit data collected over a 105-mm-HEAT (high explosive anti-tank) round. The length (head to tail) of the ordnance is 650 mm, and its body diameter is 105 mm. The object was oriented nose down and centered below the sensor array. The previous study [30] showed that this large, vertically oriented object is better represented by a two-object model.

Fig. 6(a) shows the $\log \sigma_{ii}$ versus their indexes. There is a long tail of steadily decreasing singular values, which are indicative of noise. However, in this case, the noise may not be purely Gaussian and part may arise from the approximate modeling. There is no clear gap between the large singular values and the long tail of smaller values. The question of interest pertains to the rank of the system and the number of projected channels that should be used in the TOPI.

Suppose we have two objects and assume that principal directions are independent of time. Then, the maximum r is six. In addition, it is likely that the deep main part of the object is axisymmetric, whereas the nearer surface tail end is more 3-D and scrap like. If true, then the maximum rank would be five. Irrespective an estimate of the rank r can be made by the "kink" or location of highest curvature, in the singular value-index space of Fig. 6(a). This yields $r = 7$, and it is found as marked with a cross in Fig. 6(a). This number is slightly larger than $r = 5$, or 6 assumed using the physics of the problem.

On the other hand, a useable rank can be determined by examining the TEVs. Fig. 6(b) presents the first seven and the last two TEVs. The first three TEVs look like signal vectors seen in the synthetics. They are smooth and characterized by 0, 1, and 2 zero crossings. The remaining TEVs are more erratic and are characteristic of noise. From the insight provided by the TEVs we may infer the dimension of the reduced SS is $r = 3$.

Fig. 7(a) shows the original data when Tx-13 was fired [the center transmitter, see Fig. 1(a)]. The data measured at the center receivers have large amplitudes and decay smoothly; data at edge receivers have low amplitude and are noisy. From Fig. 7(a), it is not straightforward to determine which combination of receivers and time channels should be used as input to the inversion.

The projected data are shown in Fig. 7(b). As expected from our synthetic analysis, the maximum amplitude data are associated with the first few singular vectors, and in particular, the first one. A more detailed look is provided by Fig. 7(c), which is the recorded data at Rx-1 due to an excitation of Tx-13. The data fluctuate, and responses at some time channels are larger or comparable to the responses at their preceding channels. In contrast, the projected data in Fig. 7(d) show that the first temporal channel is roughly 3.1 times as large as the maximum amplitude of the original signals and is at least around 13 times as strong as the projected signals at subsequent temporal channels. A similar phenomenon is observed in Fig. 7(e) and (f), where we show the recorded and projected data at Rx-13 from Tx-13. In this case, the projected signal at the first temporal channel is also about 3.1 times as large as the maximum amplitude of the original signals and is at least around 78 times strong as the projected data at subsequent temporal channels. This suggests that an inversion may be carried out using the projected data for the first temporal channel. This is further evident if looking

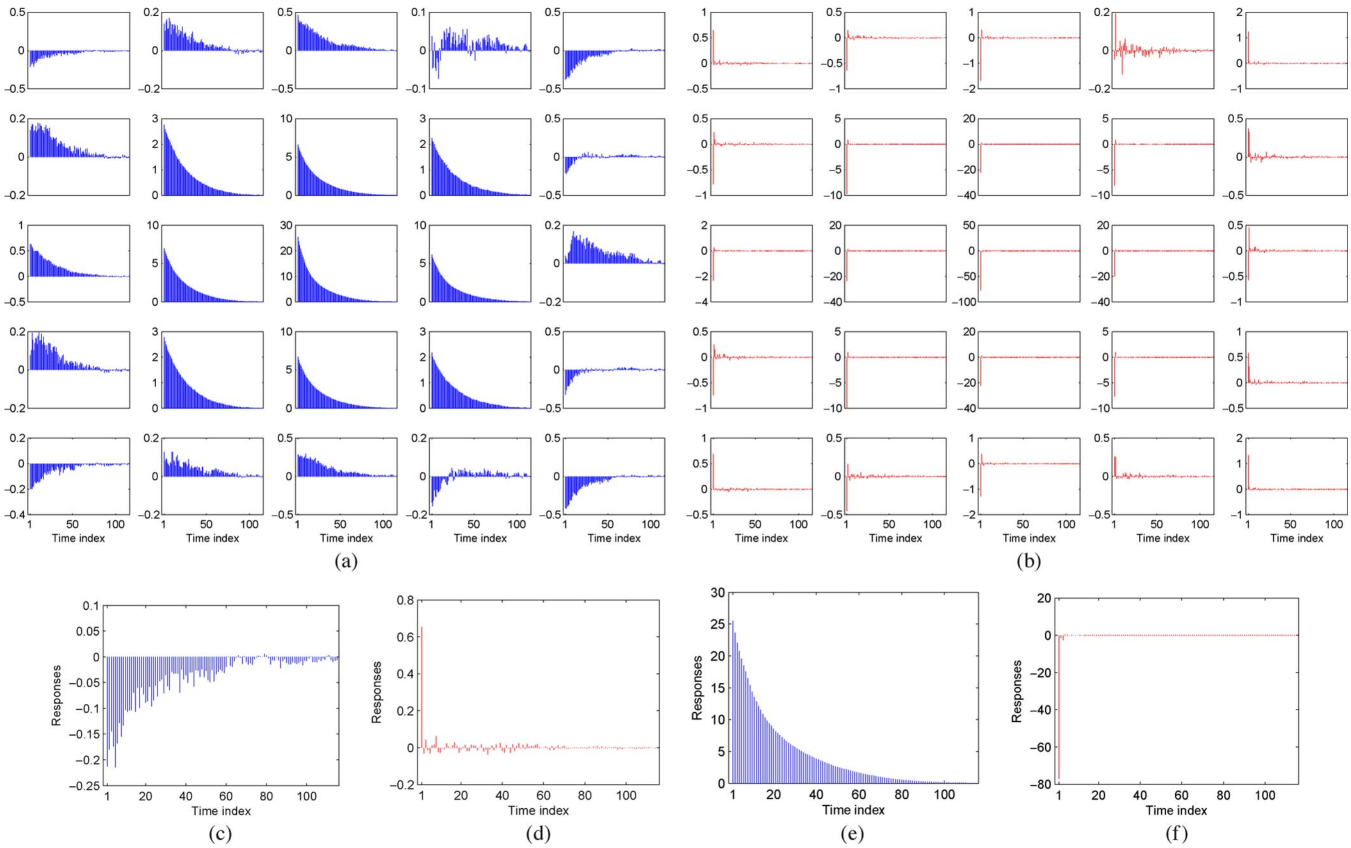

Fig. 7. Test-pit data. (a) Original data at 25 receivers with Tx-13 excitation. (b) Projected data at 25 receivers with Tx-13 excitation. (c), (d) Original and projected data of Tx-13/Rx-1 pair. (e), (f) Original and projected data of Tx-13/Rx-13 pair.

back at the singular value spectrum. The amplitudes of singular values contain the information about the importance of the eigenvectors. One notices that σ_{11} is about 18 times larger than σ_{22} and it dominates the other singular values.

As aforementioned, the determination of r was analyzed from the known physics of the problem, singular value distribution, smoothness of the temporal singular vectors, and the behavior of the projected data. Numbers varied from one to seven. To further investigate the effects of different choices, we undertake the following analysis. We first perform the TOPI with individual vectors $\mathbf{v}_j, j = 1, 2, 3, 4, 5, 6, 7$. Table I lists the inverted locations. Both $\mathbf{v}_1$ and $\mathbf{v}_2$ produce identical locations for the large object but estimated depths for the smaller item differ by 12 cm. When any single vector from $\mathbf{v}_3$ onward is used the location estimates are quite inaccurate. Next, we test the TOPI using five different subspaces $[\mathbf{v}_1, \ldots, \mathbf{v}_j]$, $j = 2, 3, 5, 7, 10$ and attain all identical locations. For this real data example, the TOPI is robust to the selection of projected channels so long as at least one of the two main singular vectors are used.

Further investigations can be carried out to observe the impact of the signal vector $\mathbf{v}_1$. We form the following subspaces by excluding $\mathbf{v}_1$, i.e., $[\mathbf{v}_2, \mathbf{v}_3]$, $[\mathbf{v}_2, \ldots, \mathbf{v}_4]$, $[\mathbf{v}_2, \ldots, \mathbf{v}_5]$, and $[\mathbf{v}_2, \ldots, \mathbf{v}_7]$. The results are summarized in Table I. All subspaces return almost the same location. The situation changes when the two major signal vectors $\mathbf{v}_1$ and $\mathbf{v}_2$ are omitted. When the TOPI is carried out with the subspaces $[\mathbf{v}_3, \mathbf{v}_4]$, $[\mathbf{v}_3, \ldots, \mathbf{v}_5]$ and $[\mathbf{v}_3, \ldots, \mathbf{v}_7]$ erratic results are obtained for $\mathbf{r}_1$ but $\mathbf{r}_2$ are consistently estimated. We conclude that the signal vectors associated with the two large singular values have information about both shallow and deep objects, whereas the next few vectors have information primarily about the shallow object.

TABLE I
TOPI WITH SINGLE $\mathbf{v}_j$ AND VARIOUS SUBSPACES IN THE REAL DATA EXAMPLE. IN THE TABLE, $V_{1j} = [\mathbf{v}_1, \ldots, \mathbf{v}_j]$, $j = 2, 3, 5, 7, 10$. $V_{2j} = [\mathbf{v}_2, \ldots, \mathbf{v}_j]$, $j = 3, 4, 5, 7$

TEVs	(x_1, y_1, z_1) (m)	(x_2, y_2, z_2) (m)
$\mathbf{v}_1$	(0.02, -0.01, -0.61)	(0.03, -0.01, -0.27)
$\mathbf{v}_2$	(0.02, -0.02, -0.61)	(0.04, -0.02, -0.15)
$\mathbf{v}_3$	(0.04, -0.33, -0.85)	(0.03, -0.33, -0.21)
$\mathbf{v}_4$	(0.26, 0.26, -0.01)	(0.26, 0.26, -0.01)
$\mathbf{v}_5$	(-0.50, -0.48, -1.20)	(-0.44, -0.50, -1.20)
$\mathbf{v}_6$	(-0.47, -0.50, -1.01)	(-0.47, -0.50, -1.01)
$\mathbf{v}_7$	(0.50, 0.26, -1.20)	(0.08, 0.56, -1.20)
V_{1j}	(0.02, -0.01, -0.60)	(0.03, -0.01, -0.26)
V_{2j}	(0.03, -0.02, -0.58)	(0.04, -0.02, -0.20)
$[\mathbf{v}_3, \mathbf{v}_4]$	(0.48, 0.36, -0.80)	(0.03, -0.03, -0.20)
$[\mathbf{v}_3, \mathbf{v}_4, \mathbf{v}_5]$	(-0.09, -0.50, -1.2)	(0.04, -0.02, -0.20)
$[\mathbf{v}_3, \cdots, \mathbf{v}_7]$	(-0.04, -0.50, -1.2)	(0.04, -0.02, -0.20)

Overall, the aforementioned tests show that the inclusion of the signal vectors $[\mathbf{v}_1, \mathbf{v}_2]$ is sufficient to recover the locations via the TOPI. This is consistent with observations in the numerical experiments. The TOPI-recovered polarizabilities are given in Fig. 8(a) and (b) for $r = 1, 7$, where the red curves represent the known polarizabilities of the 105-mm projectile, and the blue and black curves represent the recovered ones.

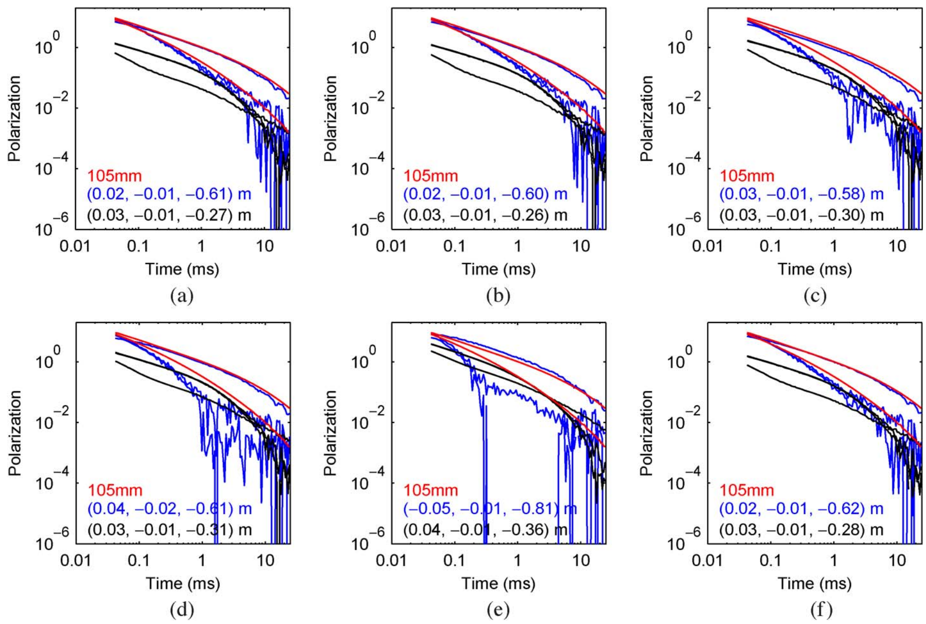

Fig. 8. Recovered polarizabilities from test-pit data. TOPI: (a) 1 TEV, (b) 7 TEVs. Inversion of original data with time channels of: (c) 115, (d) 51, (e) 16, and (f) 13. On the polarization plots, the red curves represent the known polarizabilities of 105-mm projectile and the blue and black the recovered ones.

To test the sensitivity of inversions to the selection of time channels in the original domain, we invert responses from different subsets of time channels. Generally, responses at early time channels are less prone to be noisy but the choice of the latest time to be used is difficult to assess. Here, we use responses from the first 51, 16, and 13 channels (i.e., $N_t = 51, 16, 13$), respectively. The first time channel is 0.042 ms and the last is, respectively 0.89, 0.124, and 0.101 ms. Similar to the two-object synthetic case, we also present the inversion with $N_t = 115$ time channels that are used in constructing the TOPI. Fig. 8(c)–(f) present the associated inversion results of the recovered locations and polarizabilities. Using $N_t = 115$, 51 or 16 produces less accurate results and there is substantial difference between $N_t = 16$ and $N_t = 13$. Likely, the noise is starting to become significant in that range [see Fig. 8(d) and (e)]. The result of $N_t = 115$ is somewhat better than those of $N_t = 51$ or 16 but is not optimal. In contrast, the TOPI is not sensitive to the subspace-based channel selection. In this example, the effective rank, based upon the shape of the TEVs, is estimated to be three. The TOPI returns almost identical results for inversions with rank $r = 1, 2, 3, 5, 7, 10$. This parallels the results obtained in synthetic experiments. This suggests that the new algorithm is much more robust w.r.t. the inclusion of noise vectors and has greater potential for providing a stable correct result [e.g., Fig. 8(a) and (b)].

V. Conclusion

We have considered the problem of inverting multiple time channel TEM data. Tests showed that the accuracy of source localization via a traditional nonlinear inversion can be critically dependent upon the selected time channels. To address this problem, we propose a TOPI method that circumvents either the manual choice of which channels to select or the difficult task of estimating the unknown noise. The method has four steps: 1) perform the SVD of the STRM; 2) project the STRM onto the temporal SS matrix; 3) compute source locations in the projected temporal domain; and 4) obtain target polarizabilities in the original data domain. A key step in the method is to determine the number r of temporal signal vectors used for projection. Information about r can be obtained from the spectrum of singular values, from the shape of the TEVs, from the values of the projected data, and from the fundamental physics of the problem. One feature that seems particularly diagnostic is the shape of the TEVs. Specifically, signal eigenvectors are smooth and have only a few polarity changes, with generally one additional zero crossing per unit increase in rank. Noise eigenvectors are oscillatory and have a random behavior. As a result, the projected TEM responses are associated with a few early temporal indexes, and the transformed responses are suppressed at subsequent channels. Therefore, the oscillating properties of the TEVs or highly compressed projected responses make the selection of projected temporal channels easy. Moreover, tests show that the TOPI returns almost the same result with various r values whenever signal vectors are included. In other words, the TOPI is robust to the size of a SS. In contrast, the usual inversion in the original domain is sensitive to channel selection and can derive poor results in case of inappropriate selection.

In comparison with the standard nonlinear inversion method implemented in original time-channel domain, the TOPI can be a potentially practical tool that is not only computationally efficient but also is able to produces more accurate results since a substantial portion of the noise in the data is automatically winnowed from the analysis.

Acknowledgment

The authors are thankful to the editor and reviewers for their constructive comments that help improve the manuscript.

REFERENCES

[1] Y. Das, J. E. McFee, J. Toews, and G. C. Stuart, "Analysis of an electromagnetic induction detector for real-time localization of buried objects," *IEEE Trans. Geosci. Remote Sens.*, vol. 28, no. 3, pp. 278–288, May 1990.

[2] A. Sebak, L. Shafai, and Y. Das, "Near-zone fields scattered by three-dimensinal highly conducting permeable objects in the field of an arbitrary loop," *IEEE Trans. Geosci. Remote Sens.*, vol. 29, no. 1, pp. 9–15, Jan. 1991.

[3] N. Geng, K. E. Baum, and L. Carin, "On the low frequency natural responses of conducting and permeable target," *IEEE Trans. Geosci. Remote Sens.*, vol. 37, no. 1, pp. 347–359, Jan. 1999.

[4] B. Barrow and H. H. Nelson, "Model-based characterization of electromagnetic induction signatures obtained with the MTADS electromagnetic array," *IEEE Trans. Geosci. Remote Sens.*, vol. 39, no. 6, pp. 1279–1285, Jun. 2001.

[5] J. T. Miller, T. Bell, J. Soukup, and D. Keiswetter, "Simple phenomenological models for wideband frequency-domain electromagnetic induction," *IEEE Trans. Geosci. Remote Sens.*, vol. 39, no. 6, pp. 1294–1298, Jun. 2001.

[6] T. H. Bell, B. J. Barrow, and J. T. Miller, "Subsurface discrimination using electromagnetic induction sensors," *IEEE Trans. Geosci. Remote Sens.*, vol. 39, no. 6, pp. 1286–1293, Jun. 2001.

[7] L. S. Riggs, J. E. Mooney, and D. E. Lawrence, "Identification of metallic mine-like objects using low frequency magnetic fields," *IEEE Trans. Geosci. Remote Sens.*, vol. 39, no. 1, pp. 56–66, Jan. 2001.

[8] L. R. Pasion and D. W. Oldenburg, "A discrimination algorithm for UXO using time domain electromagnetics," *J. Eng. Environ. Geophys.*, vol. 28, no. 2, pp. 91–102, 2001.

[9] L. Carin *et al.*, "On the wideband EMI response of a rotationally symmetric permeable and conducting target," *IEEE Trans. Geosci. Remote Sens.*, vol. 39, no. 6, pp. 1206–1213, Jun. 2001.

[10] H. Huang and I. J. Won, "Characterization of UXO-like targets using broadband electromagnetic induction sensors," *IEEE Trans. Geosci. Remote Sens.*, vol. 41, no. 3, pp. 652–663, Mar. 2003.

[11] Y. Zhang, L. Collins, H. Yu, C. Baum, and L. Carin, "Sensing of unexploded ordnance with magnetometer and induction: Theory and signal processing," *IEEE Trans. Geosci. Remote Sens.*, vol. 41, no. 5, pp. 1005–1015, May 2003.

[12] J. T. Smith and H. F. Morrison, "Estimating equivalent dipole polarizabilities for the inductive response of isolated conductive bodies," *IEEE Trans. Geosci. Remote Sens.*, vol. 42, no. 6, pp. 1208–1214, Jun. 2004.

[13] D. D. Snyder, D. C. George, S. C. MacInnes, and J. Torquil Smith, "An assessment of three dipole-based programs for estimating UXO target parameters with induction EM," in *Proc. SEG*, Las Vegas, NV, USA, 2008.

[14] S. L. Tantum and L. M. Collins, "A comparison of algorithms for subsurface target detection and identification using time-domain electromagnetic induction data," *IEEE Trans. Geosci. Remote Sens.*, vol. 39, no. 6, pp. 1299–1306, Jun. 2001.

[15] A. B. Tarokh, E. L. Miller, I. J. Won, and H. Huang, "Statistical classification of buried objects from spatially sampled time or frequency domain electromagnetic induction data," *Radio Sci.*, vol. 39, no. 4, Aug. 2004, RS4S05.

[16] L. R. Pasion, "Inversion of Time Domain Electromagnetic Data for the Detection of Unexploded Ordnance," Ph.D. dissertation, University of Bristish Columbia, Vancouver, CA, USA, 2007.

[17] A. Aliamiri, J. Stalnaker, and E. L. Miller, "Statistical classification of buried unexploded ordnance using nonparametric prior models," *IEEE Trans. Geosci. Remote Sens.*, vol. 45, no. 9, pp. 2794–2806, Sep. 2007.

[18] D. Williams, C. P. Wang, X. J. Liao, and L. Carin, "Classification of unexploded ordnance using incomplete multisensor multiresolution data," *IEEE Trans. Geosci. Remote Sens.*, vol. 45, no. 7, pp. 2364–2373, Jul. 2007.

[19] Q. H. Liu, X. J. Liao, and L. Carin, "Detection of unexploded ordnance via efficient semisupervised and active learning," *IEEE Trans. Geosci. Remote Sens.*, vol. 46, no. 9, pp. 2558–2567, Sep. 2008.

[20] E. Gasperikova, J. T. Smith, H. F. Morrison, A. Becker, and K. Kappler, "UXO detection and identification based on intrinsic target polarizabilities," *Geophysics*, vol. 74, no. 1, pp. B1–B9, 2009.

[21] S. D. Billings *et al.*, "Unexploded ordnance discrimination using magnetic and electromagnetic sensors: Case study from a former military site," *Geophysics*, vol. 75, no. 3, pp. B103–B114, 2010.

[22] L. Beran *et al.*, "Practical strategies for classification of unexploded ordnance," *Geophysics*, vol. 78, no. 1, pp. E41–E46, 2013.

[23] T. Bell, "Adaptive and Iterative Processing Techniques for Overlapping Signatures," Air Educ. Train. Command (AETC), Arlington, VA, USA, Mar. 1–16, 2006, report.

[24] F. Shubitidze *et al.*, "Application of the normalized surface magnetic charge model to UXO discrimination in cases with overlapping signals journal of applied geophysics," *J. Appl. Geophys.*, vol. 61, no. 3–4, pp. 292–303, 2007.

[25] F. Shubitidze *et al.*, "Applying a volume dipole distribution model to next-generation sensor data for multi-object data inversion and discrimination," in *Proc. SPIE*, 2010, vol. 7664, pp. 7664071–76640711.

[26] J. T. Miller *et al.*, "Source separation using sparse-solution linear solvers," in *Proc. SPIE*, Apr. 2010, vol. 7664, pp. 766409-1–766409-8.

[27] L.-P. Song, D. W. Oldenburg, L. R. Pasion, and S. D. Billings, "Transient electromagnetic inversion of multiple targets," *SPIE*, vol. 7303, pp. 73030R–73030R12, 2009.

[28] L.-P. Song, L. R. Pasion, S. D. Billings, and D. W. Oldenburg, "Nonlinear inversion for multiple objects in transient electromagnetic induction sensing of unexploded ordnance: Technique and applications," *IEEE Trans. Geosci. Remote Sens.*, vol. 49, no. 10, pp. 4007–4020, Oct. 2011.

[29] T. M. Grzegorczyk, B. E. Barrowes, F. Shubitidze, J. P. Fernández, and K. O'Neill, "Simultaneous identification of multiple unexploded ordnance using electromagnetic induction sensors," *IEEE Trans. Geosci. Remote Sens.*, vol. 49, no. 7, pp. 2507–2517, Jul. 2011.

[30] L.-P. Song, L. R. Pasion, and D. W. Oldenburg, "Estimating source locations of unexploded ordnance using the multiple signal classification algorithm," *Geophysics*, vol. 77, no. 4, pp. WB127–WB135, 2012.

[31] F. Shubitidze, J. P. Fernández, I. Shamatava, B. E. Barrowes, and K. O'Neill, "Joint diagonalization applied to the detection and discrimination of unexploded ordnance," *Geophysics*, vol. 77, no. 4, pp. WB149–WB160, 2012.

[32] H. H. Nelson, "EMI Array for Cued UXO Discrimination," Environmental Security Technology Certification Program (ESTCP), Alexandria, VA, USA, MM-0601, May 2008.

[33] F. S. Grant and G. F. West, *Interpretation Theory in Applied Geophysics*. New York, NY, USA: McGraw-Hill, 1965, section 6.5.

[34] J. D. Jackson, *Classical Electrodynamics*, 2nd ed. New York, NY, USA: Wiley, 1975, pp. 180–182.

[35] J. J. Moré, "The Levenberg–Marquardt Algorithm: Implementation and Theory," in *Numerical Analysis*, *Lecture Notes in Mathematics 630*, G. A. Watson, Ed. Berlin, Germany: Springer-Verlag, 1977, pp. 105–116.

[36] T. F. Coleman and Y. Li, "An interior, trust region approach for nonlinear minimization subject to bounds," *SIAM J. Optim.*, vol. 6, no. 2, pp. 418–445, May 1996.

[37] R. A. Horn and C. R. Johnson, *Matrix Analysis*. Cambridge, U.K.: Cambridge Univ. Press, 1985, pp. 402–404.

[38] G. H. Golub and C. F. Van Loan, *Matrix Computations*, 2nd ed. Baltimore, MD, USA: The Johns Hopkins Univ. Press, 1989, pp. 139–147.

Authors' photographs and biographies not available at the time of publication.